RSC Advances

ROYAL SOCIETY OF CHEMISTRY

www.rsc.org/advances

RSC Advances

PAPER

Single Etch Fabrication and Characterization of Robust Nanoparticle Tipped Bi-Level Superhydrophobic Surfaces

Abinash Tripathy*[a], Girish Muralidharan[b], Amitava Pramanik[b] and Prosenjit Sen*[a]

Though hierarchical roughness gives best anti-wetting surfaces, their performance degrades quickly as nanostructures fail even under small mechanical stresses. Using spin coated alumina nanoparticles as etch mask we report a single-etch based wafer-scale fabrication of robust nanoparticle tipped superhydrophobic surfaces with dual-level roughness. The top-level structures in the dual-level roughness provides mechanical robustness and the surface maintains its liquid repellency even when damaged due to mechanical shear. This complex dual-level structure leads to interesting droplet bouncing dynamics which was studied for several fluids. Though the normalized spread diameter showed good agreement with previous reports, we observed dependence of contact time on both surface wettability and impact velocity. By breaking the impact event into spreading, recoil and detachment we show that the variation in contact time is mostly in the detachment phase. Contact time variation with impact velocity is attributed to partial impalement of the top-level nanostructures which increases the contact line stiction. For highest impact velocity while water droplets rebound completely, Xanthum gum droplets having similar surface tension and hysteresis leaves residual droplets on surfaces with higher solid fraction which is contrary to the current understanding. Large range of shear-rate dependent viscosity in conjunction with partial impalement explains this new observation.

1. INTRODUCTION

Superhydrophobic surfaces have become an important and popular topic of research over the last decade due to their ability to repel fluids[1–3] which enables their use in applications like drag reduction[4,5] anti-icing[6–8], antibacterial[9–12], and self-cleaning surfaces[13–16]. One of the challenges in these applications is to maintain the Cassie-Baxter state of fluid repellency by preventing transition to the Wenzel state due to impalement, even at extreme droplet impact conditions characterized by high velocities and low temperatures. Several studies investigating natural and artificial superhydrophobic surfaces have now established the benefits of hierarchical roughness in design of surfaces with extreme fluid repellency[17–20]. Hierarchical superhydrophobic structures are commonly fabricated using a two-step process[21–23] where micron-scale features is formed first using a lithographic technique. This is followed by decorating the micron-scale features with nanoscale roughness. The common disadvantage of these surfaces arises due to the fragile nature of the nanostructures against shear, limiting their use in real world applications[24]. To address this problem, mechanically robust bi-level superhydrophobic surfaces comprising of taller microcones and shorter nanograss[25] have been demonstrated recently. These bi-level structures were formed using a two-step etch process in a cryogenic deep reactive ion etching (DRIE) tool.

In this work, we report fabrication of a bi-level superhydrophobic surface but using only a single etch step in a conventional DRIE. In order to keep the fabrication costs low, the developed process does not use lithography or any other complex patterning technique. The developed process is based on spin coating followed by a single etch step which leads to a randomly distributed bi-level superhydrophobic surface, where the taller features are tipped with alumina nanoparticles. Due to their high hardness, chemical inertness and insulation properties the alumina nanoparticles are expected to provide enhanced stability to the prepared surface. Alumina nanoparticle tipped nano pillars are also envisaged to provide enhanced antimicrobial functionality[26].

Under static conditions superhydrophobic surfaces have high contact angle and low contact angle hysteresis. For investigating sturdiness against Cassie-to-Wenzel transition during droplet impact, a well proven technique involves characterizing the impact dynamics using high speed imaging to quantify contact time and maximum spread diameter[27–30]. Initial studies[31,32] provided the threshold impact velocity for droplet impalement by balancing capillary pressure with the dynamic pressure ($\propto \rho V^2$). Later studies attributed Cassie-to-

[a] Centre for Nano Science and Engineering (CeNSE), Indian Institute of Science, Bangalore-560012, India
[b] Unilever R&D Bangalore, 64, Main Road, Whitefield, Bangalore 560066, India

† Electronic supplementary information (ESI) available: Texts and figures describing details about the fabrication, characterization of different surfaces. Video S1 and S2 showing the abrasion test and self-cleaning behaviour of the nanostructured superhydrophobic surface respectively. Video S3 showing droplet dynamics of different liquids on 0.1 alumina weight% superhydrophobic substrate released from a height of 7 cm. Video S4 and S5 showing droplet dynamics of different liquids on 0.2 weight% alumina and 1 weight% alumina superhydrophobic substrates released from a height of 28 cm.

Wenzel transition observed at lower than threshold impact velocity to water hammer pressure, which arises due to the shock wave generated during the sudden deceleration of the droplet. Better resistance of the hierarchical structures against Cassie-to-Wenzel transition was attributed by McCarthy *et al.* [17] to the role of nanostructures in supporting higher dynamic pressure and the role of microstructures in limiting the propagation of the water hammer pressure. Based on experimental data Dash *et al.*[33] determined the value of the water hammer pressure coefficient to be two orders of magnitude smaller than that for a flat surface. For low viscosity liquids, the droplets deform just before impact due to compression of the trapped air. Maitra *et al.*[22] have attributed the high pressure ring-like edge arising from the interface deformation for failure of superhydrophobicity. Recently *Lee et al.*[34] have identified late stage overpressure during recoil as a reason for failure of micro-structured surfaces. The above studies, however do not account for variation of the contact time with surface wettability. Li *et al.*[35] reported variation in contact time on textured surfaces and attributed it to a thin film of liquid remaining on the surface. Antonini *et al.*[36] have studied droplet impact on various nanostructured surfaces and concluded that the rebound time increased with decreasing receding contact angles. They however do not provide any insight towards the underlying physical mechanism that leads to the increase in the rebound time. Studies have also been carried out to significantly reduce the contact time of an impacting droplet on superhydrophobic surfaces with micron scale gradient features[37,38].

Though several studies have explained various physical phenomena effecting the dynamics of droplet impact on designed micro, nano and hierarchical structures there is a lack of similar investigations on random bi-level superhydrophobic structures. In order to fill this gap we characterized the droplet impact behaviour on these surfaces. For this study, in addition to water, aqueous PEG and Xanthan gum solutions (also referred as Xanthum in this work) were also used for drop impact studies on surfaces with varying wettability. The use of PEG helps in reducing the surface tension and its use in consumer to medicinal products has been well documented. In the same line, especially in the food industry, viscosity modulation is achieved through the help of addition of small quantities of Xanthan gum. By changing the height of droplet release, Weber number was varied from 15 to 250. The normalized maximum spread for the droplet matched well with other observations[39]. The contact time for our experiments showed variation with surface wettability and impact velocity. This we attribute to the special two level structure of our superhydrophobic surface. The surface interaction plays a critical role during the retraction phase of the impact. Partial failure of the top level structures at higher impact velocities leads to a difference in surface wettability, which effects the droplets retraction dynamics and hence the contact time also changes.

2. MATERIALS AND METHODS

Device Fabrication

Schematic of device fabrication is shown in **Figure S1** (Supplementary Information). Silicon wafers were cleaned in piranha solution (H_2SO_4 and H_2O_2) for 10 minutes at 90°C, followed by a HF dip for 40 seconds. The wafers were rinsed in deionized water, dried using N_2 and then baked on a hot plate at 250°C for 10 minutes. Different weight percentage (0.1%, 0.2%, 0.5% and 1%) of alumina nanoparticle (300 nm size) solutions were prepared by mixing alumina nanoparticles with ethanol followed by sonication for 15 minutes to ensure proper dispersion. Prepared nanoparticle solutions were spin coated on the silicon substrates and the remaining ethanol was removed through baking on a hot plate at 250°C for 15 minutes. The alumina nanoparticles remaining on the substrate act as a mask during the Deep Reactive Ion Etching (DRIE) process. An optimized recipe was developed to etch substrates with varying alumina nanoparticle coverage to fabricate surfaces with different wettability. The optimized nano-grass etch recipe is based on standard recipes[40–42] and uses an etch step of 7 seconds with SF_6/O_2 flow rates of 150/15 sccm and a platen power of 12-15 watts. The ICP coil power was 620 watts for both etch and passivation steps. The passivation step was 6 seconds long with C_4F_8 flow rate of 120 sccm. A total of 30 cycles of etch and passivation steps were used to form the surfaces. The fluorocarbon passivation step of the modified Bosch process was sufficient to make our surfaces superhydrophobic and a separate hydrophobic coating step was not required. SEM images of nanoparticle tipped superhydrophobic silicon surfaces for different weight % of alumina nanoparticle solutions are shown in **Figure S3** (Supplementary Information).

Image Analysis for Surface Characterization

SEM images were analyzed using ImageJ[43] to extract position and area of the nanoparticle-tipped pillars (see **Figure S4** Supplementary Information). From the top view SEM images it is difficult to distinguish between the nano-grass and single nanoparticle-tipped pillars with radius of ~ 0.25 µm or smaller. This leads to an error in the effective area fraction calculation. This error is however expected to be low due to the negligible contribution of the pillars with smaller radius to the overall area fraction as they are present in fewer numbers, which is also evident from other SEM images.

For calculation of stability of meniscus against impalement we adopt a technique similar to Samaha et al.[44]. Information of the post positions extracted from the SEM images was used to construct a Voronoi diagram (see **Figure S4** Supplementary Information). In this diagram each post has a surrounding cell, which consists of points, which are closest to it than any other post. This information is used to approximately estimate the capillary pressure for failure of the meniscus as $P_c = \gamma L_{Pillar} cos\theta_R / A_{cell}$, where L is the interface length of the post and A is the area of the Voronoi cell.

Surface Abrasion and Self-cleaning Test

The abrasion tests were performed by placing a 50 gram weight on the substrate and sliding it over a sandpaper with a

grit size of 400 (see Supplementary **Video S1**). After sliding for a distance of 60 cm, contact angle hysteresis was measured to characterize the degradation of the surfaces. This routine was repeated four times to give a total sliding distance of 240 cm for all samples. Self-cleaning tests were performed using MnO_2 powder. The surfaces were completely cleaned leaving no residues when sprayed with water (see Supplementary **Video S2**).

Droplet Impact Studies

For this study five liquids of industrial significance were selected (i) Water, (ii) 2% Polyethylene glycol (PEG), (iii) 5% PEG, (iv) 0.25% Xanthan gum (Xanthum), and (v) 0.5% Xanthan gum. PEG allows altering the surface tension of water significantly while Xanthan gum allows tuning the viscosity by an order of magnitude even at low concentrations. The properties of the different liquids used are provided in **Table S1** (Supplementary Information). A custom made tilting goniometric setup was used to measure the contact angle and hysteresis. To ensure repeatability all the measurements were repeated three times.

Droplet impact on the prepared superhydrophobic surfaces was captured using a high-speed camera (Photron FastCam SA4) at 10,000 fps (time resolution of 0.1 ms) using an experimental set up as shown in **Figure S7** (Supplementary Information). The droplets were created using a micropipette and released from six different heights (3.5 cm, 7 cm, 10 cm, 12 cm, 15 cm and 28 cm), thereby allowing variation of Weber number ($We = \rho V^2 D/\gamma$) from 15 to 250. Droplet diameters used in the calculations were measured form the captured videos. The results discussed in this work summarize 360 different experiments. Individual frames from the droplet bouncing movies were extracted and analyzed using custom software to obtain various parameters like droplet center of gravity, contact diameter and contact time.

3. RESULTS AND DISCUSSIONS

Dual Level Surface

Different weight percentage alumina nanoparticle (300 nm) solutions were spin coated on the wafer to act as an etch mask during the subsequent DRIE etch. As seen in **Figure 1** the developed process leads to a nanoparticle tipped nano-pillars. The rapid nature of the spin coating process leads to a non-uniform distribution of the nano particles on the wafer surface. We also observe aggregation of the nanoparticles leading to effective pillar diameters varying from ~300 nm to ~10 µm. As seen in the SEM images a dense silicon nano-grass with smaller height is visible between the sparsely distributed nanoparticle-tipped nano-pillars. Silicon nano-grass etching in a conventional DRIE is generally carried out in a regime where there is a delicate balance between the etch step and the passivation step. This allows the existing inhomogeneity on the wafer to act as the mask for the nano-grass etching. The inhomogeneity can arise from the variation in the thickness of the native oxide, variation of the passivation, existing contamination, or micro-masking from sputtering of an existing mask. The wide distribution in the height of the nano-grass as seen in the SEM images is a strong indication that for our case they are formed due to micro-masking during the etch process. This micro-masking is attributed to the redisposition of the sputter etch products of the alumina nanoparticle hard mask. This idea is supported by the observed reduction in the size of the alumina nanoparticles after etch as seen in the SEM micrographs. It is interesting to note that the etched surfaces show structures at two scales only for surfaces created with solutions having less than 1 weight % alumina nanoparticles. Absence of nano-grass for higher weight percentage solutions can be attributed to the reduction in etch loading leading to excess etch species, which in turn results in undercut of the formed nano-grass.

Each surface was statistically characterized using SEM images from 8 random locations on the sample using the same magnification which captured an area of 98 µm x 65 µm per image. The nanoparticle-tipped pillars were identified manually and analyzed using ImageJ[43] as seen in **Figure S4** (Supplementary Information). As seen in **Figure 2** for surfaces prepared with 0.1%, 0.2% and 0.5% solutions the distribution of the pillar radius is similar with an increase in the number of total pillars as the concentration of the nanoparticles in the solution is increased. In the analyzed area the radius distribution peaked around 0.75 µm and then reduced sharply to single digit numbers for pillars with radius 2.5 µm and above. For surfaces fabricated using 1% alumina nanoparticle solution we observe a larger degree of aggregation leading to significantly more pillars with larger radius as evident in the histogram. Effective solid fraction ϕ_{eff} for the random multi-level surface was calculated from the images assuming that for static conditions the liquid is completely supported by the top-level nanoparticle-tipped pillars. Fitting the measured contact angle data to the Cassie-Baxter equation $cos\theta^* = -1 + \phi(1 + cos\theta_Y)$ the contact angle on a flat surface with plasma coated fluorocarbon is estimated to be $\theta_Y \cong 106°$. Increase in ϕ_{eff} also leads to a dramatic increase in the contact angle hysteresis. For water, an increase of alumina weight percentage from 0.1% to 1% leads to a decrease in the contact angle from 171° to 153° and a dramatic increase in contact angle hysteresis from 1.5° to 19° (see **Figure S5** and **Figure S6** Supplementary Information). This work demonstrates a wafer scale single etch technique to fabricate dual level superhydrophobic surface which provides a simple way to tune the superhydrophobicity (water repellency) by changing the weight percentage of alumina nanoparticle solution.

Robustness of the Surface

The robustness of the prepared substrates was verified using the abrasion test with an applied normal pressure of 1.4 kPa. Contact angle hysteresis measurements using water droplets at regular intervals show a steady decrease in the repellency as shown in **Figure 3**. The surfaces prepared using 0.1%, 0.2% and 0.5% alumina solutions however retained their superhydrophobicity even after a total sliding distance of 240 cm. The SEM image in **Figure 3** confirms that the shear induced damage is restricted to the top-level posts only. The damage

seems to be a combination of tip loss and toppled pillars. The toppled tips expose their hydrophobic coated sidewalls to the droplet interface, which in combination with the unharmed nano-grass incur only a small penalty on the water repellency. In comparison there was a drastic decrease in the water repellency of the surface fabricated using 1% alumina solution. This behaviour can be understood from previous works where it has been demonstrated that for surfaces having wider posts the expected failure mechanism is through mechanical loss of the tip. The contact angle remains high as the Cassie state is maintained due to the hydrophobic coating on the sidewalls. The contact angle hysteresis however increases as the mechanical tip loss replaces the hydrophobic fluorocarbon coated top with a hydrophilic SiO_2 top. This also explains the large increase in hysteresis (~ 10°) after the first 60 cm for the surface fabricated using 1% alumina solution.

The surfaces are also chemically robust as there was only a 4° degradation in contact angle of the surface fabricated using 0.1 weight % solution after a 30 min treatment in 98% concentrated H_2SO_4 solution (**Figure 3)**. The acid treatment lead to a negligible increase in the contact angle hysteresis from 1° to 2°.

Droplet Impact Studies

Maximum Spread Diameter

Droplets impacting solid surfaces have been observed to undergo various morphological transformations such as spreading, recoil, and bouncing depending on the nature of substrate and the liquid [39,45–47]. **Figure 4** shows the snapshots of impact for droplets of different liquids on 0.1% surface released from a height of 7 cm at various time points (see **Video S3** supplementary information). A droplet of initial diameter D_0 spreads on impact with the nano-structured surface and attains a maximum spreading diameter D_{max}. For the high Weber numbers, it is well known that the kinetic energy of the droplet on impact is transformed to the surface energy and internal flows leading to $D_{max} \propto D_0 We^{1/4}$. **Figure 4** plots the normalized spread diameter for all surfaces. A linear fit on the log-log plot gives a slope of 0.26, illustrating a good match with theory. As expected for low viscosity fluids (water and PEG solutions) at these ranges of high impact velocities where the impact factor ($P = We/Re^{0.8}$) is less than one ($P < 0.4$ in our experiments), there is no significant effect of either the surface or liquid viscosity on the normalized spread diameter. Xanthum's case is interesting as its viscosity at low concentrations shows a large dynamic range[48] varying from ~10^4 at low shear rates (10^{-1} s^{-1}) to ~10 at high shear rates (10^3 s^{-1}). Just before impact the viscosity is high near the zero-shear viscosity associated with the residual oscillation from the droplet formation process. As the droplet spreads and the contact-line velocity increases, the viscosity reduces approaching infinite-shear viscosity. Even though Xanthan gum's viscosity at highest shear rates is ~10 times that of water, the impact factor[30] (*P*) in our experiments remains comparatively small with a maximum value of $P \cong 1.4$, which explains why the effect of viscosity is not observed on the maximum spread diameter.

Contact Time

The capillary energy stored in the stretched droplet causes the droplet to recoil and bounce off the superhydrophobic surface. The time that a bouncing droplet spends in contact with the surface (i.e. contact time) has been shown by several studies including the initial works of Okumura et al.[27] and Richard et al.[28] to be proportional to inertial-capillary time scale $\tau_i \propto (\rho R^3/\gamma)^{1/2}$ with a prefactor of 2.6. On designed micro-pillar surfaces their experiments further showed the independence of the contact time on droplet impact velocity for higher impact velocities ($We \geq 1$). The random nature of our surface makes the impact dynamics on the multi-level random superhydrophobic surface a complex phenomenon which is evident from the observed increase in contact time with surface wettability as seen in **Figure 4**. It is important to note that in previous studies[35,36] similar increase in contact time with surface wettability was only observed for surfaces with large contact angle hysteresis (> 5°). In contrast we observe increase in contact time even for surfaces fabricated using 0.1 weight % and 0.2 weight % solutions having contact angle hysteresis less than 5°.

In order to study this complex retraction dynamics, we calculate the variation in droplets center of gravity and the contact diameter with respect to time. We separate the impact event into three different phases as shown in **Figure 5**. The first phase covers the droplet spreading and is represented by the spread time. The second phase represented by recoil time is associated with the conversion of the stored interfacial energy in the flattened droplet back to kinetic energy leading to rapid contact line retraction. This stage ends when most of the stored interfacial energy has been converted back to the kinetic energy of the recoiling droplets and its center of gravity is approximately at $D_0/2$. In this regime the droplet retraction is modeled as inertial dewetting of thin films[49] giving a relation for recoil time as

$$\frac{\tau_r}{\tau_i} \propto \sqrt{\frac{1}{\pi(1-\cos\theta_R)}} \qquad 1$$

In the final stage that is represented by the detachment time, the inertia of the droplet drives it upward while droplet adhesion pins the contact line leading to the stretching of the droplet. Once the interfacial forces arising from the stretched droplet overcomes the droplet adhesion, the detachment of the droplet interface from the surface progresses at a rapid speed. This mechanism is verified by calculating the contact line velocity (see **Figure S8** supplementary Information) from the captured data. The contact line velocity first increases and then reaches a maximum during the droplet recoil. As the droplet approaches the spherical shape, the excess interfacial energy driving the retracting contact line reduces and the contact line velocity decreases. Finally as forces due to the stretching of the droplet overcomes the stiction forces, the contact line velocity increases till detachment. Adhesion

energy associated with the detachment is given by $\pi R^2\{\gamma_{SA} + \gamma - \gamma_{SL}\}$. This in combination with energy loss due to contact angle hysteresis leads to a total energy required for detachment as $\pi R^2\gamma(1 + cos\theta_R)$. The droplet deceleration due to adhesion and hysteresis forces can be approximated as

$$a \propto \frac{\gamma}{\rho R^2}(1 + cos\theta_R) \quad \mathbf{2}$$

With *U* being the effective velocity representing the kinetic energy of the recoiling droplet and assuming a displacement of order *R* required for detachment will lead to a detachment time in the order of

$$\tau_d \propto \frac{R}{U} + \frac{\gamma}{2\rho U^3}(1 + cos\theta_R) \quad \mathbf{3}$$

For the inertial-capillary regime the velocity *U* scales as $\sqrt{\gamma/\rho R}$ giving

$$\frac{\tau_d}{\tau_i} \propto A + B(1 + cos\theta_R) \quad \mathbf{4}$$

where A and B are constants.

Spread time, recoil time and detachment time for all experiments is summarized in **Figure 5**. The spread time is constant within the limits of experimental accuracy and is independent of the Weber number or surface. The recoil time also shows minimal variation with Weber number. The surface effect is however visible for surface fabricated using 1 weight % alumina solution having a larger recoil time compared to surfaces fabricated using 0.1 weight % solution. **Figure 6** plots the normalized recoil time as a function of $f(\theta_R) = 1/\sqrt{\pi(1 - cos\theta_R)}$. Despite of the noise we observe a trend of increase in the recoil time with reduction in receding contact angle. As seen in **Figure 5** most of the observed variation in contact time for an impact can be attributed to the variation in the detachment time. It is also evident that the detachment time for surfaces created with 1% alumina solution is visibly larger than the other surfaces. In this phase of bouncing where the residual droplet inertia works against viscous dissipation and contact line stiction, it is natural that the detachment time strongly depends on the droplet adhesion. This is evident in plot of the normalized detachment time with $g(\theta_R) = (1 + cos\theta_R)$ as shown in **Figure 6**.

Significant noise observed in both **Figure 6 (a)** and **(b)** is attributed to the random nature of the substrates. For our random dual level surface this variation in contact time is attributed to variations in impalement of top-level nanoparticle-tipped pillars which leads to increased surface adhesion and longer contact times. Several phenomena have been identified for impalement of superhydrophobic surfaces. For the random bi-level surface reported here the top-level structures due to their sparse nature are not able to support the liquid interface at higher impact velocities. The interaction of the liquid with the top-level structures, however leads to a rapid relaxation of the excess pressures allowing the bottom-level nano-grass to effectively repel the liquid interface and prevent complete Cassie to Wenzel transition which is verified from the absence of residual liquid on the surface for impact velocities up to 1.72 m/s ($We < 130$). For case of surfaces prepared using 1% solution we also observe an increase in the contact time with the Weber number (see **Figure 4**) especially at higher impact velocities. For the surface created using 1% solution the increased impalement of the surface at higher Weber number leads to a rapid increase in the effective solid fraction as seen in **Figure 6 (d)**.

Maitra et al.[22] have also observed similar increase in rebound times for micro/hierarchical superhydrophobic surfaces at sub-freezing temperatures only. The increase was attributed to partial impalement of the structures near the zone of impact at higher Weber number and subsequent increase in viscous effects due to rapid cooling of the impaled liquid. This case is however different as the increase in contact time is observable at room temperature and is attributed to the increase in contact line stiction.

Non-Newtonian Fluids

At the highest impact speed of 2.3 m/s in our experiments we observe residual droplets in some cases as shown in **Table 1**. As expected for liquids with lower surface tension (PEG solutions) Cassie to Wenzel transition happens at a lower critical velocity and residual droplets are observed on all surfaces. In contrast water with higher surface tension is repelled on all surfaces. Higher surface tension enhances the capillary forces that support the liquid interface and resists wetting. Despite of the high surface tension of Xanthan gum solutions we observed residual droplets due to wetting of the nanostructures for surfaces with higher solid fraction (0.5% and 1%). This is in contrary to the expectation and other observations where lower solid fraction surfaces fail first due to their lower anti-wetting capillary pressures. For Xanthan gum solutions the shear-rate dependent viscosity and associated losses play a major role in the de-wetting phase, which is clearly evident in **Figure 4** where the recoiling Xanthan gum droplets show reduced necking and surface waves. During the recoil and detachment phase as the shear-rates decrease the viscosity increases. Dramatic increase in the local viscosity between the wetted top-level structures makes retraction of the liquid interface from the partially impaled surface energetically unfavorable. This energy cost associated with viscous effects increases for higher wt% surfaces and explains why Xanthan gum droplets leave residual droplets whereas water droplets with similar surface tension and contact angle hysteresis rebound completely (see **Video S4** and **S5** Supplementary Information).

4. CONCLUSION

A simple wafer-scale, single etch DRIE process has been used to fabricate bi-level random nanoparticle tipped nano-structured surfaces with varying wettability by changing the alumina nanoparticle solution concentration. The bi-level structure provides enhanced robustness against shear which is demonstrated using the sandpaper abrasion test. The surface is further verified to show self-cleaning behaviour and are demonstrated to be robust against acid (H_2SO_4) attack. In

order to understand its wetting behaviour a statistical analysis of the surface is done to extract solid fraction from the SEM images. The normalized contact time and normalized spreading diameter of water and other liquids (aqueous PEG and Xanthum solutions) were measured on the fabricated surfaces with varying wettability. We observe contact time to be dependent on the wettability of the superhydrophobic surface. We analyze the droplet impacts by breaking the event into three phases as spreading, recoil and detachment. The variation of contact time is traced to detachment phase of the bouncing event where the inertia of the pinned droplet causes it to stretch. When the interfacial energy in the stretched droplet overcomes the contact line stiction, the detachment takes place. The bi-level nature of our superhydrophobic surface also leads to variation in contact time with velocity at higher Weber numbers due to increased partial impalement of the top level nano-structures. For liquids with strong shear-rate dependent viscosity the partial impalement of the structures leads to stagnant high-viscosity liquid trapped between the impaled top-level structures. This significantly increases the energy required to de-wet the top-level structures and explains the observed residual droplets for Xanthum gum. In comparison water under same conditions with similar contact angle hysteresis and surface tension does not leave any residual droplets.

CORRESPONDING AUTHORS

Abinash Tripathy, Email: atripathy90@cense.iisc.ernet.in
Prosenjit Sen, Email: prosenjits@cense.iisc.ernet.in

CONFLICT OF INTEREST

The authors declare no competing financial interest.

ACKNOWLEDGEMENT

The authors would like to thank Unilever R&D, Bangalore for the financial support.

REFERENCES

1 X. Gao and L. Jiang, *Nature*, 2004, **432**, 36–36.
2 D. Quéré, *Reports Prog. Phys.*, 2005, **68**, 2495–2532.
3 T. 'Leo' Liu and C.-J. 'CJ' Kim, *Science (80-.).*, 2014, **346**, 1096–1100.
4 C. H. Choi and C. J. Kim, *Phys. Rev. Lett.*, 2006, **96**, 1–4.
5 C. Lee and C. J. Kim, *Phys. Rev. Lett.*, 2011, **106**, 1–4.
6 L. Mishchenko, B. Hatton, V. Bahadur, J. A. Taylor, T. Krupenkin and J. Aizenberg, *ACS Nano*, 2010, **4**, 7699–7707.
7 A. J. Meuler, G. H. Mckinley and R. E. Cohen, *ACS Nano*, 1845, **4**, 7048–7052.
8 S. Jung, M. K. Tiwari, N. V. Doan and D. Poulikakos, *Nat. Commun.*, 2012, **3**, 615.
9 E. P. Ivanova, J. Hasan, H. K. Webb, V. K. Truong, G. S. Watson, J. A. Watson, V. A. Baulin, S. Pogodin, J. Y. Wang, M. J. Tobin, C. Löbbe and R. J. Crawford, *Small*, 2012, **8**, 2489–2494.
10 E. P. Ivanova, J. Hasan, H. K. Webb, G. Gervinskas, S. Juodkazis, V. K. Truong, A. H. F. Wu, R. N. Lamb, V. A. Baulin, G. S. Watson, J. A. Watson, D. E. Mainwaring and R. J. Crawford, *Nat. Commun.*, 2013, **4**, 1–7.
11 J. Hasan, S. Raj, L. Yadav and K. Chatterjee, *RSC Adv.*, 2015, **5**, 44953–44959.
12 K. Ostrikov, M. Macgregor-Ramiasa, A. Cavallaro, K. (Ken) Ostrikov and K. Vasilev, *J. Phys. D. Appl. Phys.*, 2016, **49**, 304001.
13 R. Blossey and C. Scientifique, 2003, 301–306.
14 A. Tuteja, W. Choi, M. Ma, J. M. Mabry, S. a Mazzella, G. C. Rutledge, G. H. McKinley and R. E. Cohen, *Science*, 2007, **318**, 1618–1622.
15 X. Deng, L. Mammen, H.-J. Butt and D. Vollmer, *Science (80-.).*, 2012, **335**, 67–70.
16 W. Barthlott and C. Neinhuis, *Planta*, 1997, **202**, 1–8.
17 Y. Kwon, N. Patankar, J. Choi and J. Lee, *Langmuir*, 2009, **25**, 6129–6136.
18 M. McCarthy, K. Gerasopoulos, R. Enright, J. N. Culver, R. Ghodssi and E. N. Wang, *Appl. Phys. Lett.*, 2012, **100**, 1–6.
19 I. D. Jung, M. C. Lee, H. Lim, E. Smela and J. S. Ko, *Appl. Surf. Sci.*, 2015, **349**, 705–714.
20 X. Chen, Y. Gong, D. Li and H. Li, *Colloids Surfaces A Physicochem. Eng. Asp.*, 2016, **492**, 19–25.
21 H. Kim, C. Lee, M. H. Kim and J. Kim, *Langmuir*, 2012, **28**, 11250–7.
22 T. Maitra, M. K. Tiwari, C. Antonini, P. Schoch, S. Jung, P. Eberle and D. Poulikakos, *Nano Lett.*, 2014, **14**, 172–182.
23 B. Bhushan, Y. C. Jung and K. Koch, *Philos. Trans. A. Math. Phys. Eng. Sci.*, 2009, **367**, 1631–1672.
24 J. Lv, Y. Song, L. Jiang and J. Wang, *ACS Nano*, 2014, **8**, 3152–3169.
25 V. Kondrashov and J. Rühe, *Langmuir*, 2014, **30**, 4342–50.
26 M. J. Hajipour, K. M. Fromm, A. Akbar Ashkarran, D. Jimenez de Aberasturi, I. R. de Larramendi, T. Rojo, V. Serpooshan, W. J. Parak and M. Mahmoudi, *Trends Biotechnol.*, 2012, **30**, 499–511.
27 K. Okumura, F. Chevy, C. Clanet, D. Richard and D. Quere, 2002, **237**, 237–243.
28 D. Richard, C. Clanet and D. Quéré, *Nature*, 2002, **417**, 811.
29 D. C. Roux, J. J. Cooper-White, G. H. McKinley and V. Tirtaatmadja, *Phys. Fluids*, 2003, **15**, S12.
30 C. Clanet, C. Béguin, D. Richard and D. Quéré, *J. Fluid Mech.*, 2004, **517**, 199–208.
31 D. Bartolo, F. Bouamrirene, E. Verneuil, A. Buguin, P. Silberzan and S. Moulinet, *Europhys. Lett.*, 2006, **74**, 299–305.
32 M. Reyssat, a Pépin, F. Marty, Y. Chen and D. Quéré, *Europhys. Lett.*, 2007, **74**, 306–312.
33 S. Dash, M. T. Alt and S. V. Garimella, *Langmuir*, 2012, **28**, 9606–9615.
34 C. Lee, Y. Nam, H. Lastakowski, J. I. Hur, S. Shin, A.-L. Biance, C. Pirat, C.-J. 'Cj' Kim and C. Ybert, *Soft Matter*, 2015, **11**, 14–17.
35 X. Li, X. Ma and Z. Lan, *Langmuir*, 2010, **26**, 4831–4838.
36 C. Antonini, F. Villa, I. Bernagozzi, A. Amirfazli and M. Marengo, *Langmuir*, 2013, **29**, 16045–16050.
37 Y. Liu, L. Moevius, X. Xu, T. Qian, J. M. Yeomans and Z. Wang, *Nat. Phys.*, 2014, **10**, 515–519.

38 Y. Liu, G. Whyman, E. Bormashenko, C. Hao and Z. Wang, *Appl. Phys. Lett.*, 2015, **107**.

39 A. L. Yarin, *Annu. Rev. Fluid Mech.*, 2006, **38**, 159–192.

40 H. Jansen, M. de Boer, R. Legtenberg and M. Elwenspoek, *J. Micromechanics Microengineering*, 1995, **5**, 115.

41 K. H. Chen, C. H. Hsu, H. C. Lo, S. Chattopadhyay, C. T. Wu, J. S. Hwang, D. Das and L. C. Chen, *Tamkang J. Sci. Eng.*, 2004, **7**, 129–134.

42 Y.-F. Huang, S. Chattopadhyay, Y.-J. Jen, C.-Y. Peng, T.-A. Liu, Y.-K. Hsu, C.-L. Pan, H.-C. Lo, C.-H. Hsu, Y.-H. Chang, C.-S. Lee, K.-H. Chen and L.-C. Chen, *Nat. Nanotechnol.*, 2007, **2**, 770–774.

43 C. a Schneider, W. S. Rasband and K. W. Eliceiri, *Nat. Methods*, 2012, **9**, 671–675.

44 M. A. Samaha, H. Vahedi Tafreshi and M. Gad-el-Hak, *Phys. Fluids*, 2011, **23**, 0–8.

45 B. L. Scheller and D. W. Bousfield, *AIChE Journal, 41(6)*, 1995, **41**, 1357–1367.

46 V. Bergeron, D. Bonn, J. Martin and L. Vovelle, *Nature*, 2000, **405**, 772–5.

47 L. Xu, W. W. Zhang and S. R. Nagel, *Phys. Rev. Lett.*, 2005, **94**, 1–4.

48 P. J. Whitcomb, *J. Rheol. (N. Y. N. Y).*, 1978, **22**, 493.

49 D. Bartolo, C. Josserand and D. Bonn, *J. Fluid Mech.*, 2005, **545**, 329.

FIGURES AND TABLES

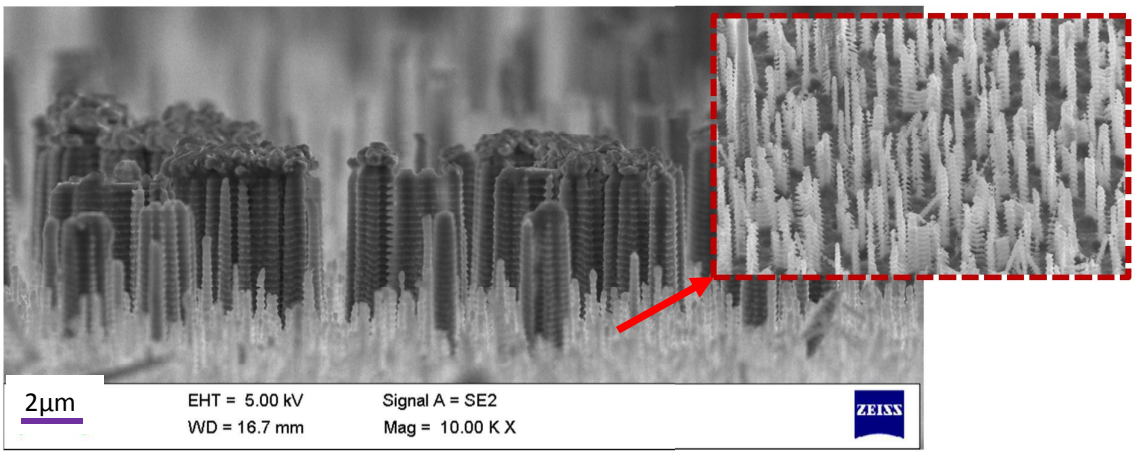

0.5% alumina surface nanoparticle tipped pillars and silicon nano-grass

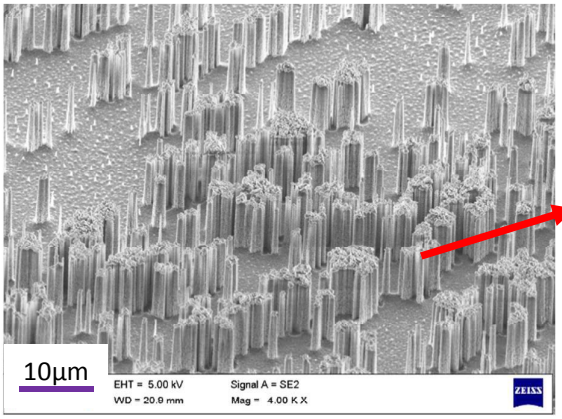

Silicon nano-grass is absent on surface made using 1% alumina solution

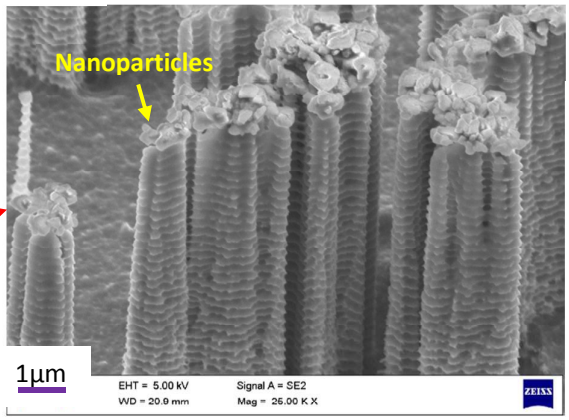

Nanoparticle tipped pillars

Figure 1: Representative SEM images of nano structured superhydrophobic silicon surface for different weight % of alumina nanoparticle solution. For low weight % a sparse distribution of the nanoparticle tipped pillars is obtained. A nano-grass of lower height is also observed in-between the nanoparticle tipped pillars. While the nanoparticle tipped pillars provides mechanical robustness, presence of silicon nano-grass in the space between the pillars provides resistance against liquid fill-in. For surfaces created with 1% alumina nanoparticle solution the nano-grass is not present between the nano-pillars.

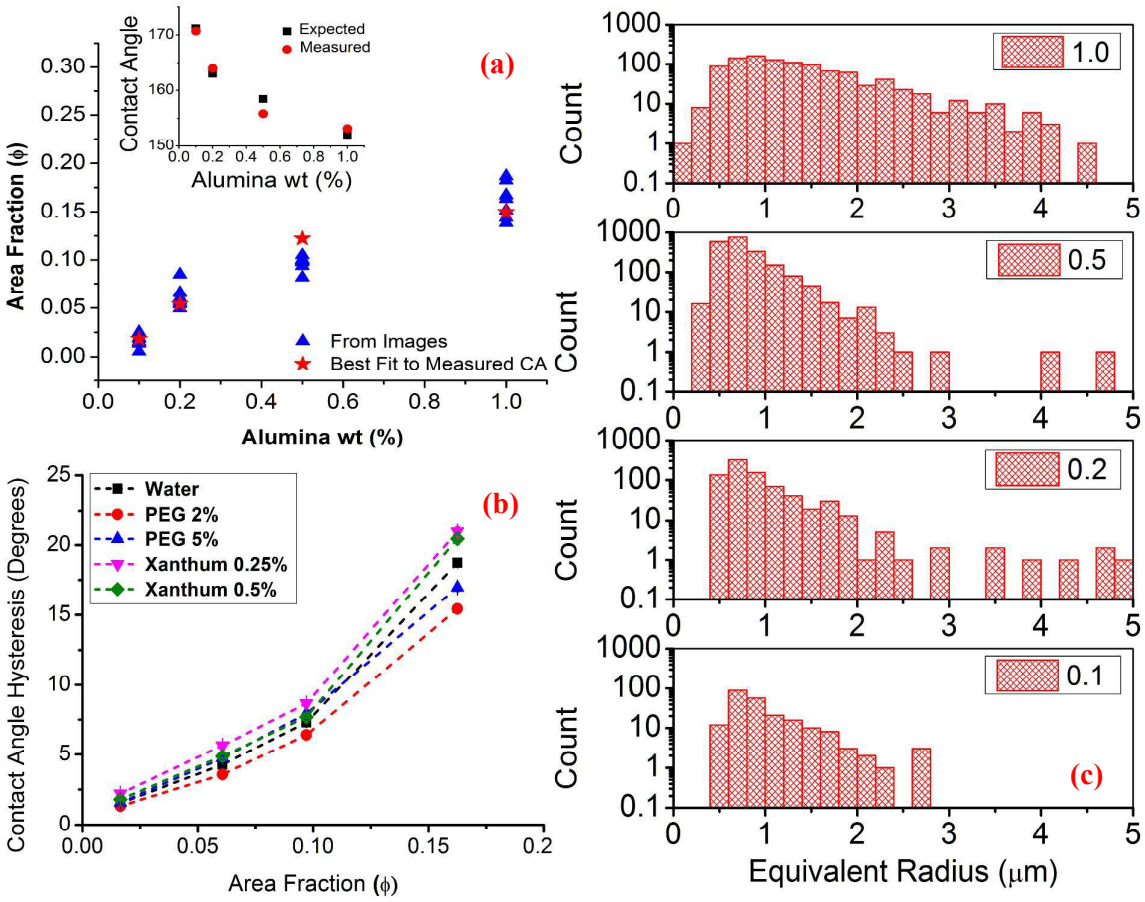

Figure 2: (Top Left) Area fraction as measured from SEM images and as estimated from the best fit to the measured contact angle values for water. (Bottom left) Measured contact angle hysteresis of different liquids on the different surfaces. By varying the concentration of the alumina nanoparticles surfaces with varying area fraction and hence adhesion as measured using contact angle hysteresis is obtained. (Right) Histogram of the equivalent radius for the alumina nanoparticle tipped pillars.

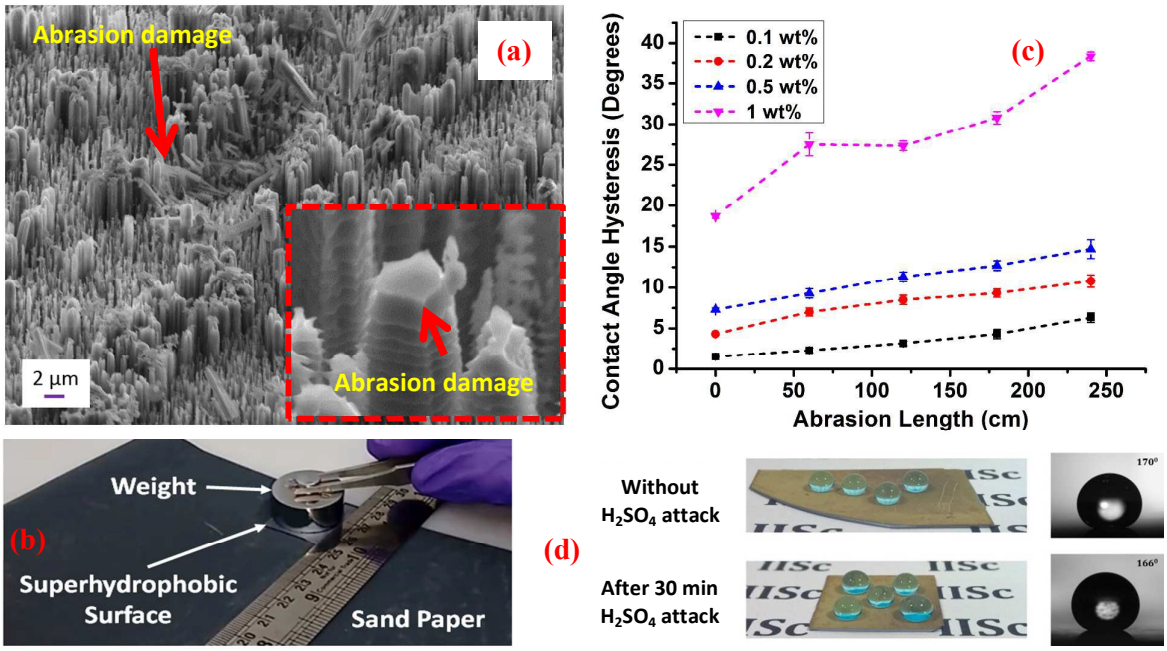

Figure 3: (Top left) SEM images showing abrasion damage to the 0.5 wt % surface. (Top right) Surface degradation with abrasion is characterized using contact angle hysteresis measurements. Loss in water repellency is minimal even after 240 cm abrasion over sandpaper (400 grit) with 1.4 kPa pressure. (Bottom left) Prepared surface changes minimally even after a 30 min dip in concentrated (98%) H_2SO_4. (Bottom right) Image of the abrasion test.

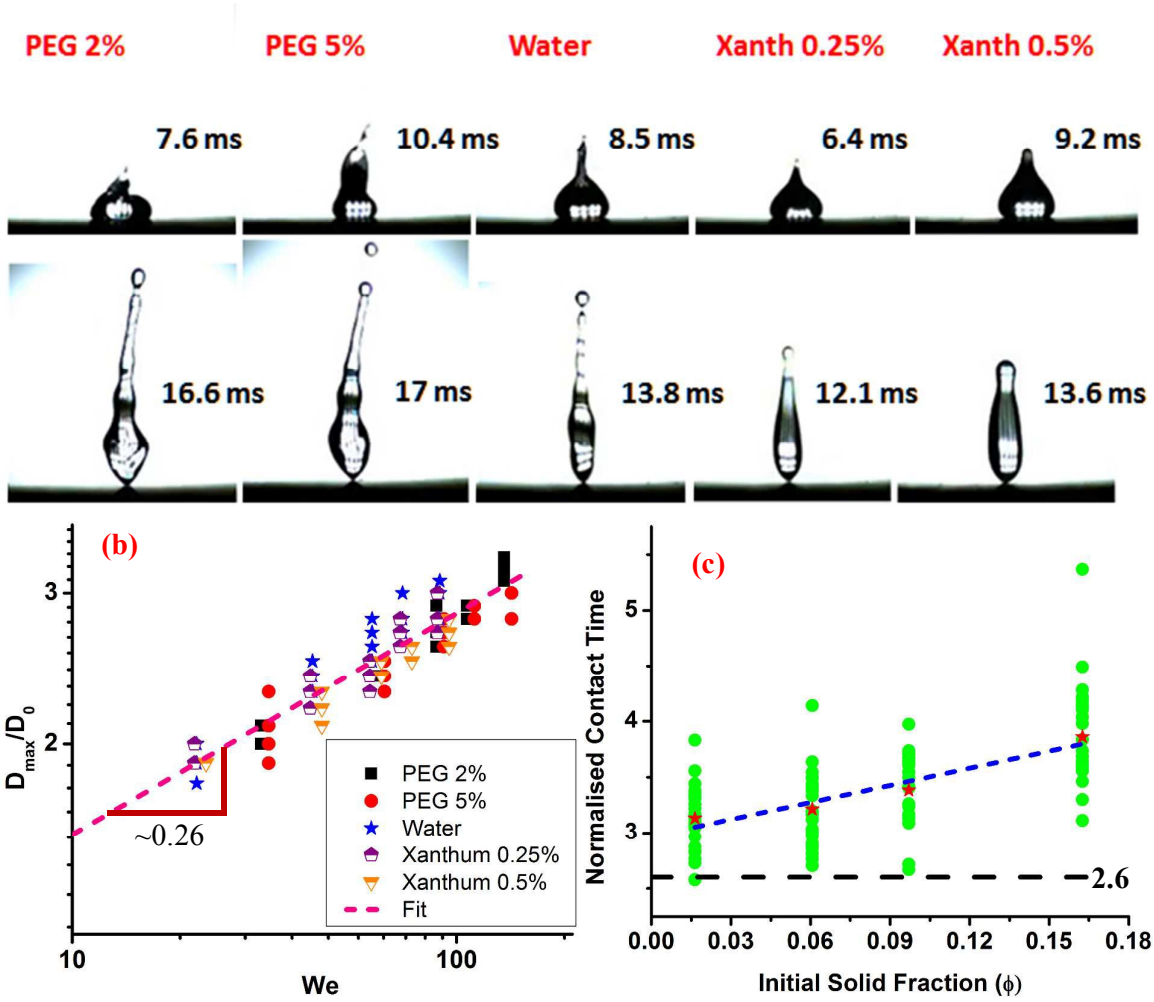

Figure 4: High speed images of impact of different liquid droplets released from a height of 7 cm on surfaces created with 0.1 weight % alumina coated surfaces. (b) Log-Log plot of normalized spread diameter vs. Weber number for all liquids on all surfaces. The fit shows a good fit with existing theory. (c) Normalised contact time as a function of the weight percentage of alumina solution used for fabricating the surface. Red stars show the group mean. Dashed line shows a linear fit for all the data.

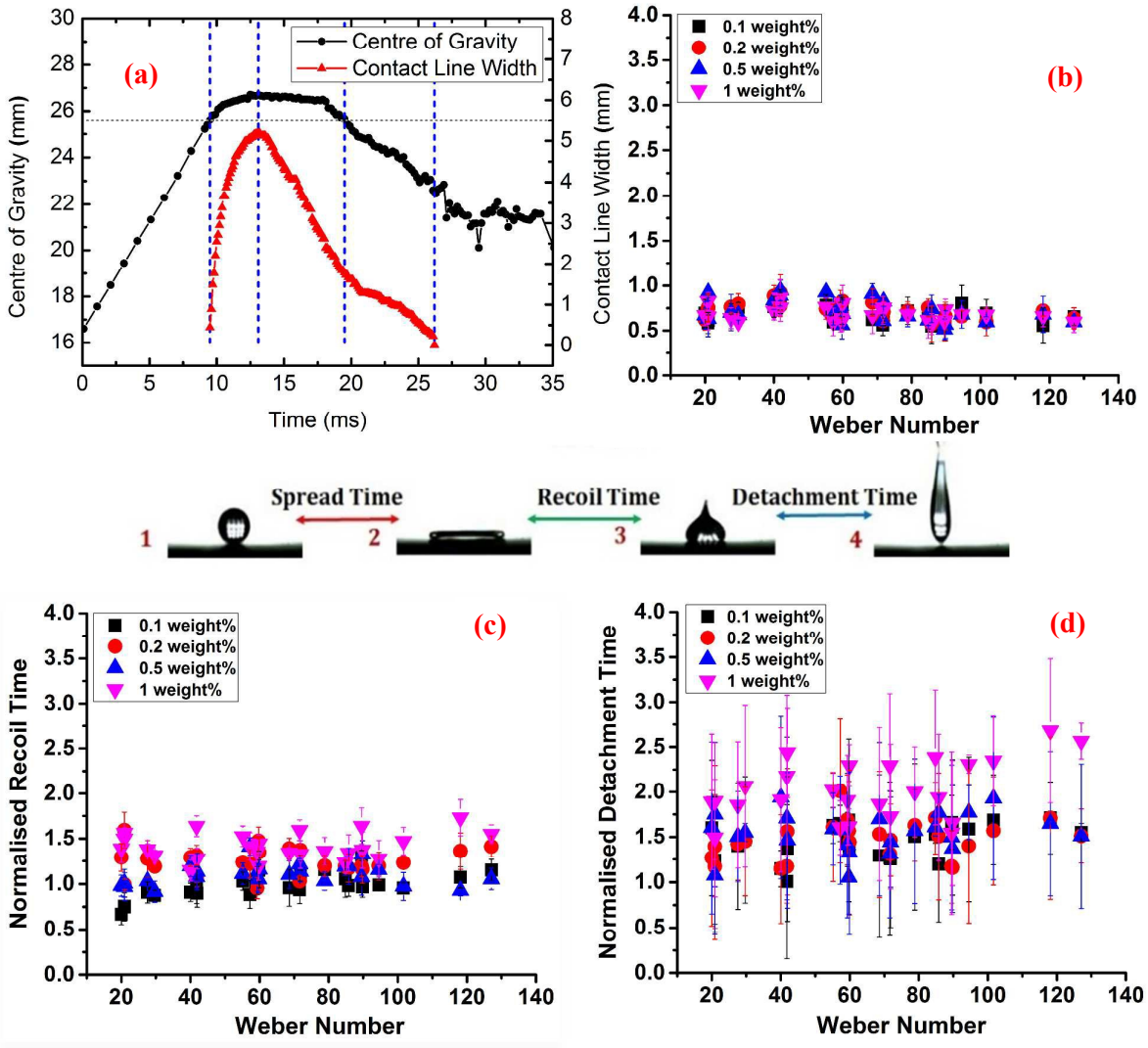

Figure 5: (a) Time variation of centre of gravity and contact line width of the droplet during impact. Extracted from image analysis. (b) Normalised spread time versus Weber number for various liquids on all surfaces. Spread time is constant within the accuracy of the experiments. (c) Normalised recoil time shows small variation but the surface effect is evident. (d) Normalised detachment time vs. Weber number for all experiments. Larger detachment times for surfaces fabricated with 1 weight % solution is due to its large contact angle hysteresis. Large variation in detachment time for all surfaces and liquids is attributed to the variation of contact line force for our random superhydrophobic surface.

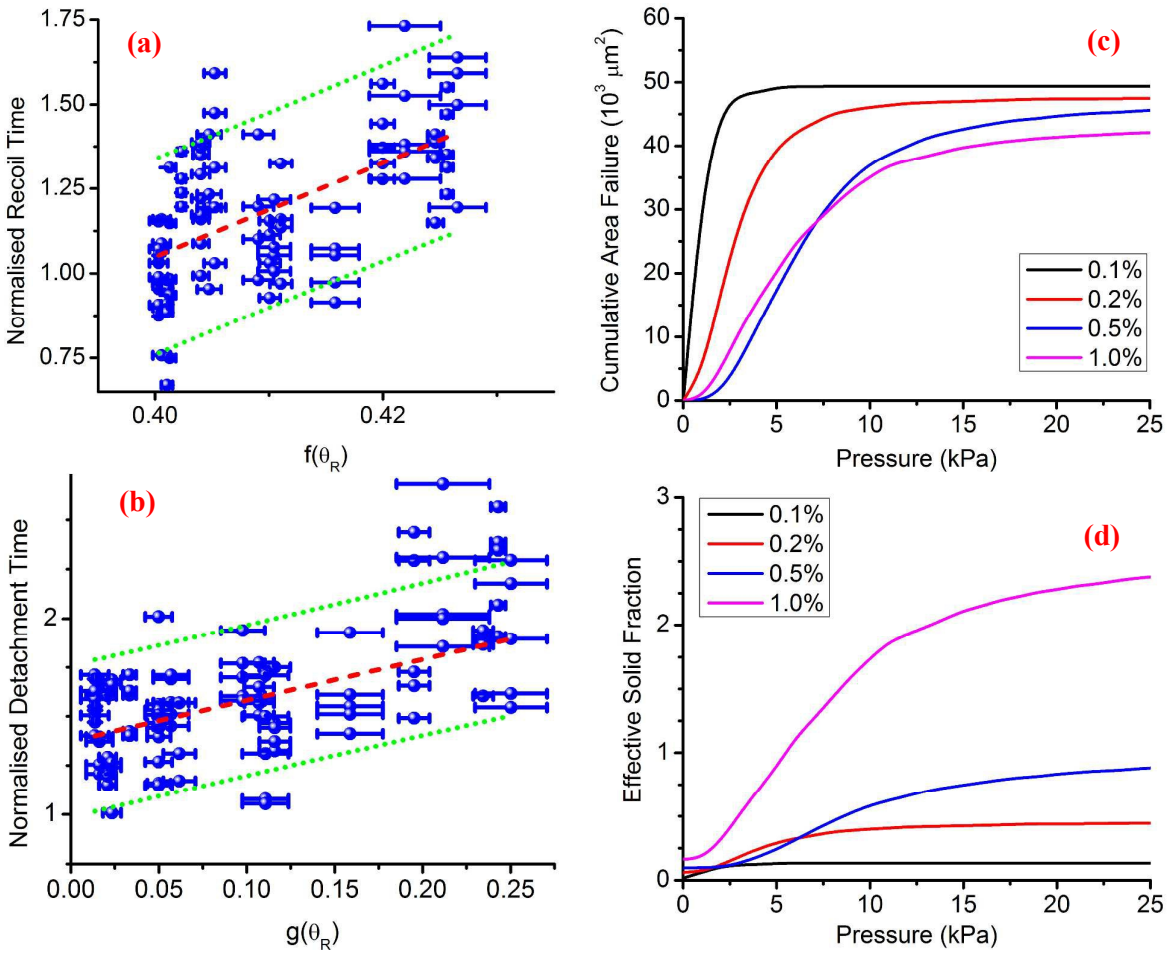

Figure 6: (a) Normalised recoil time. The dashed lines are provided as guides. (b) Normalised detachment time. The detachment time increases at lager Webber numbers and larger hysteresis. (c) Cumulative area failure due to liquid pressure as calculated from the SEM image analysis. (d) Effective solid fraction due to partial impalement at different pressures as calculated from SEM image analysis.

Table 1: Trend of surface failure leading to residual liquid for impact velocity of 2.3 m/s

		PEG 5%	PEG 2%	Xanth. 0.5%	Water	Xanth. 0.25%
	ϕ_{eff}	53.4 mN/m	55.8 mN/m	70.9 mN/m	72 mN/m	73.8 mN/m
0.1 wt%	**0.0264**	YES	YES	NO	NO	NO
0.2 wt%	**0.0778**	YES	YES	NO	NO	NO
0.5 wt%	**0.1758**	YES	YES	YES	NO	YES
1 wt%	**0.2158**	YES	YES	YES	NO	YES

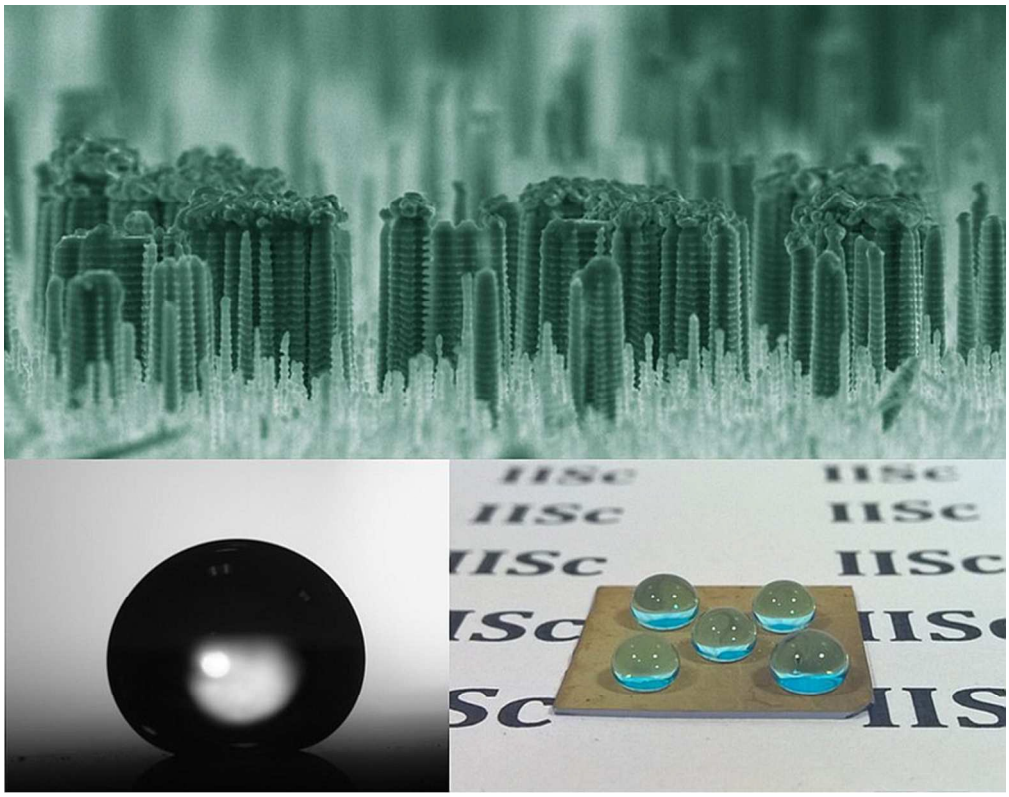

70x55mm (300 x 300 DPI)